# MIT Open Access Articles

## *Multi-cation perovskites prevent carrier reflection from grain surfaces*

# Multi-cation perovskites prevent carrier reflection from grain surfaces

Makhsud I. Saidaminov[1,5,6], Kristopher Williams[2,6], Mingyang Wei[1,6], Andrew Johnston[1], Rafael Quintero-Bermudez[1], Maral Vafaie[1], Joao M. Pina[1], Andrew H. Proppe[1,3], Yi Hou[1], Grant Walters[1], Shana O. Kelley[3,4], William A. Tisdale[2]* and Edward H. Sargent[1]*

The composition of perovskite has been optimized combinatorially such that it often contains six components ($A_x B_y C_{1-x-y} Pb X_z Y_{3-z}$) in state-of-art perovskite solar cells. Questions remain regarding the precise role of each component, and the lack of a mechanistic explanation limits the practical exploration of the large and growing chemical space. Here, aided by transient photoluminescence microscopy, we find that, in perovskite single crystals, carrier diffusivity is in fact independent of composition. In polycrystalline thin films, the different compositions play a crucial role in carrier diffusion. We report that methylammonium (MA)-based films show a high carrier diffusivity of $0.047 \, cm^2 \, s^{-1}$, while MA-free mixed caesium-formamidinium (CsFA) films exhibit an order of magnitude lower diffusivity. Elemental composition studies show that CsFA grains display a graded composition. This curtails electron diffusion in these films, as seen in both vertical carrier transport and surface potential studies. Incorporation of MA leads to a uniform grain core-to-edge composition, giving rise to a diffusivity of $0.034 \, cm^2 \, s^{-1}$ in CsMAFA films. A model that invokes competing crystallization processes allows us to account for this finding, and suggests further strategies to achieve homogeneous crystallization for the benefit of perovskite optoelectronics.

Perovskite solar cells (PSCs) have recently reached a certified power conversion efficiency (PCE) of 25.2% (refs. [1–10]). This has been enabled in substantial part by combinatorial optimization of the constituents of the perovskite ($ABX_3$) active layer[11–16]. State-of-art PSCs incorporate a remarkable six or more components when the A site contains a mixture of Cs, MA ($CH_3NH_3^+$) and FA ($HC(NH_2)_2^+$) with a mixture of Br and I on the X site[17–21].

The simultaneous presence of Cs and FA is needed to maintain an average tolerance factor that favours a stable perovskite structure[19]. The MA component is, in principle, not required for stability; yet the best-performing perovskite devices contain at least 5% MA[22–24]. Earlier studies attributed the role of cation mixing to the suppression of carrier recombination centres[20], whereas recent studies correlate it with the homogeneous distribution of halogens[25,26]. How precisely mixed cations and halides contribute to the crystallization dynamics, and, ultimately, to the performance of perovskite materials, remains a matter of ongoing investigation. Incomplete understanding works against continued improvements in perovskite composition in view of the huge combinatorial chemical space available.

Here, we use transient photoluminescence microscopy (TPLM) to image the diffusion of charge carriers in perovskite single crystals and thin films, all as a function of composition. In single crystals, we find—strikingly—that carrier diffusivity is independent of composition. In contrast, composition plays a major role in thin films—the architecture relevant to solar cell applications. We also observe that diffusivity in films decreases with decreasing MA content, and that the presence of Br and Cs induces inhomogeneous crystallization in MA-free CsFA films.

Using energy dispersive X-ray (EDX) and X-ray photoemission spectroscopy (XPS), we report that this inhomogeneous crystallization forms grains with a graded composition. Kelvin probe force microscopy (KPFM) shows that the cores trap charge carriers within a high-potential-barrier shell, and vertical photoluminescence (PL) quenching and transient photocurrent reveal that this corresponds to curtailed electron diffusion in these films. Incorporation of MA leads to a uniform grain core-to-edge composition, achieved by balancing competing crystallization pathways, allowing carriers to move more readily from grain to grain.

## Transient PL microscopy for carrier diffusion imaging
To study the spatiotemporal carrier dynamics in perovskites of different compositions, we employed TPLM[27]. The layout of this experiment is shown in Fig. 1a. A pulsed laser source is focused onto the sample surface using a microscope objective lens to a spot size of ~1 μm. Epifluorescence from the distribution of carriers excited by the laser is collected by the objective lens and sent to a telescopic relay lens which projects an image of the sample fluorescence onto an image plane. An avalanche photodiode is raster scanned across the image plane to detect the change of the fluorescence intensity in both space and time.

To establish the applicability of TPLM for perovskites, we first visualized carrier dynamics in single crystals of $MAPbI_3$, the most studied perovskite composition to date[28,29]. Supplementary Video 1 shows the experimental result from TPLM, normalized to a peak value for each frame in time; Fig. 1b shows selected frames of the video. The size of the spot increases with time due to the diffusion of

[1]Department of Electrical and Computer Engineering, University of Toronto, Toronto, Ontario, Canada. [2]Department of Chemical Engineering, Massachusetts Institute of Technology, Cambridge, MA, USA. [3]Department of Chemistry, University of Toronto, Toronto, Ontario, Canada. [4]Department of Pharmaceutical Sciences, Leslie Dan Faculty of Pharmacy, University of Toronto, Toronto, Ontario, Canada. [5]Present address: Department of Chemistry and Electrical & Computer Engineering, Centre for Advanced Materials and Related Technologies (CAMTEC), University of Victoria, Victoria, British Columbia, Canada. [6]These authors contributed equally: Makhsud I. Saidaminov, Kristopher Williams, Mingyang Wei. *e-mail: tisdale@mit.edu; ted.sargent@utoronto.ca
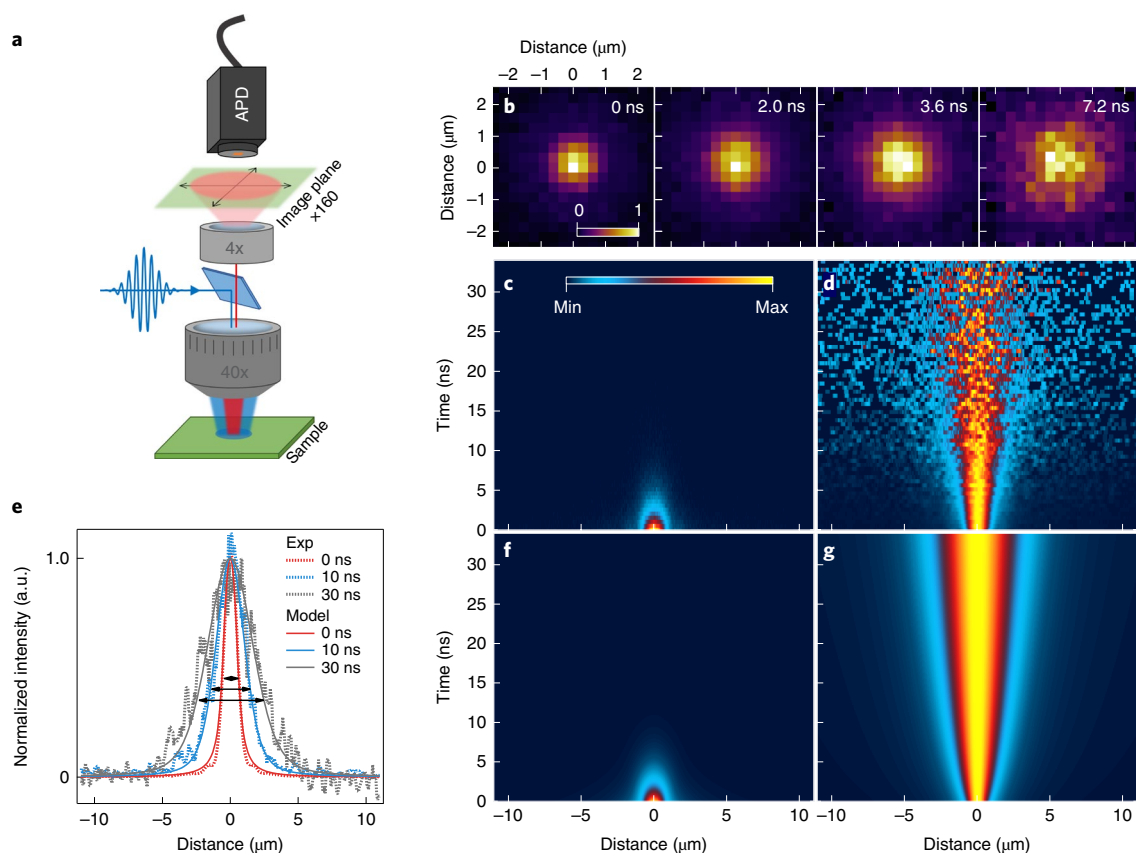
**Fig. 1 | TPLM. a**, Schematic of the experimental set-up. **b**, Experimental two-dimensional TPLM images on an MAPbI$_3$ single crystal at 0, 2.0, 3.6 and 7.2 ns after excitation. **c,d**, Experimental one-dimensional diffusion images for uncorrected (**c**) and normalized data (**d**) at each time point. **e**, Slices from the one-dimensional data (dotted lines) and model fits (solid lines) at 0, 10 and 30 ± 5 ns that show broadening of carrier distribution in time. **f,g**, Corresponding uncorrected (**f**) and normalized (**g**) simulation data used to extract diffusion constant. APD, avalanche photodiode; Exp, experimental.

carriers and the spot exhibits isotropic growth. The isotropy of diffusion perpendicular to the detection plane (sample depth) was confirmed in PL quenching experiments (Supplementary Method 2.1).

Because of the isotropic nature of carrier diffusion in perovskites, we track carrier diffusion in one dimension without loss of information; this enables higher-resolution data better suited to quantitative analysis. Figure 1c shows raw data from a one-dimensional scan across the laser spot. Since it is difficult to visualize diffusion due to the decaying fluorescence signal, the same data, normalized in time, are shown in Fig. 1d. Here, it is clear that the width of the spot is increasing with time, attributable to carrier diffusion from the excitation spot (note that bimolecular recombination alone also contributes to the broadening—see Supplementary Method 1.5). Slices through the intensity profile at different time intervals show that the full width at half maximum (FWHM) of the spot has changed from 1.2 μm to 4.1 μm within the first 30 ns of excitation (Fig. 1e).

To extract the diffusion constant of carriers, the data were modelled using the following partial differential equation:

$$\frac{\partial N}{\partial t} = D\nabla^2 N - AN - BN^2 - CN^3 \tag{1}$$

where $N = N(x, y, z, t)$ is the spatial distribution of carrier density in time, $D$ is the spatial diffusion constant, $A$ is the trapping rate constant, $B$ is the radiative decay constant and $C$ is the Auger recombination rate constant. Importantly, we observe that the measured PL intensity scales quadratically with the incident laser power, indicating that the PL signal arises from recombination of free electrons and holes generated by the laser pulse

(and not bound excitons or photogenerated minority carriers that have encountered majority carriers—see Supplementary Method 1.1 and Supplementary Fig. 1). Consequently, we make the simplifying assumption that the electron and hole density are locally equivalent and that the diffusivity $D$ is the isotropic ambipolar diffusivity. Photon recycling[30] is neglected as simulations show the effect to be small for the analysis carried out at or near the main PL peak (Supplementary Method 1.8).

Solutions to equation (1) were obtained using the explicit finite difference method (EFDM) with boundary conditions that include surface recombination[31] (see Supplementary Methods 1.2 and 1.3). The output of the model was shown to be rigorous (see Supplementary Method 1.7) and fed into a multivariate fit of the experimental data. We note that the generation rate of laser pulse (0.59 ns FWHM) does not affect the fitting parameters, and hence was not included in the multivariate fit of the diffusion data: this reduces the number of parameters required by the model (Supplementary Method 1.6). From the extracted values of the diffusion and decay parameters, we calculate the diffusion length of carriers, $L_D$, according to the following equation:

$$L_D = \sqrt{2D\tau} \tag{2}$$

where $\tau$ is the carrier lifetime at low excitation fluence. In this case, the intensity-independent lifetime is given by $\tau = A^{-1}$.

We used this model to fit all single crystal and thin film data (see Supplementary Table 1). The results of this method for MAPbI$_3$ single crystals are shown in Fig. 1f and Fig. 1g for the raw and normalized model output, respectively. The carrier diffusivity and
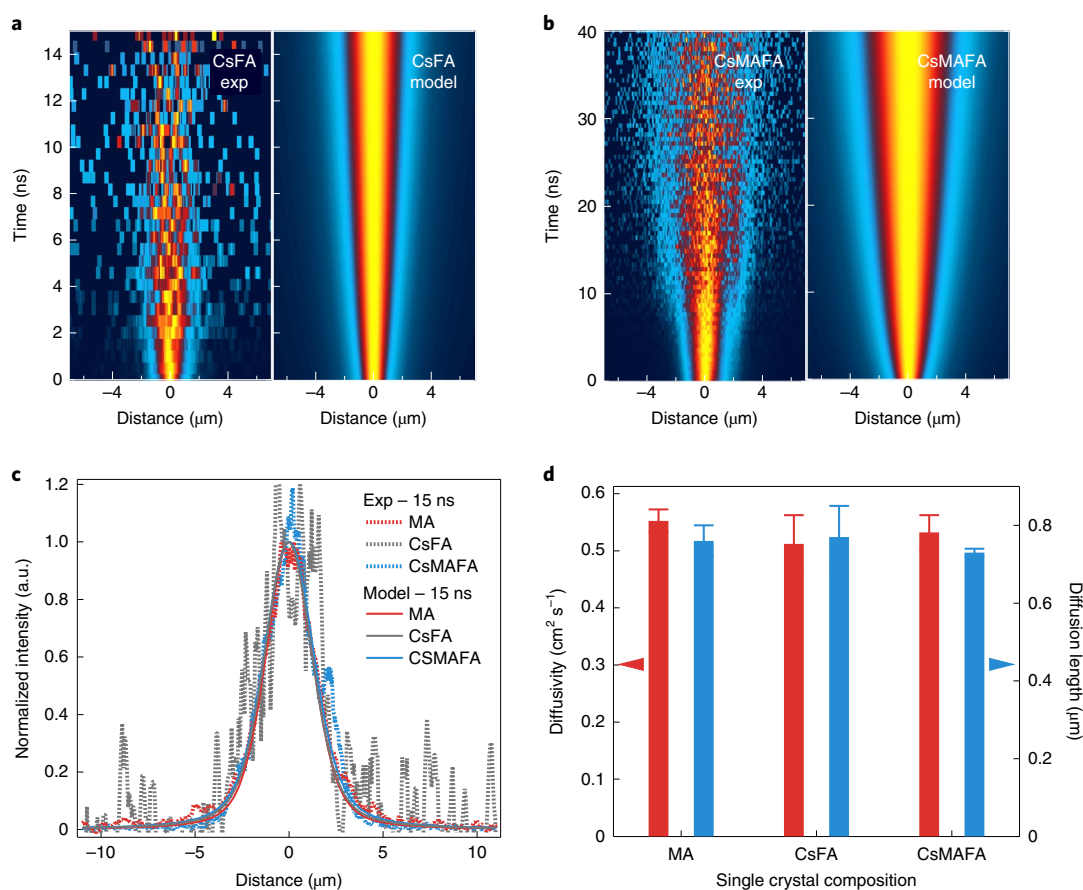
**Fig. 2 | Carrier diffusion in single crystals as a function of composition. a,b,** Normalized experimental and simulated carrier diffusion images for (**a**) CsFA and (**b**) CsMAFA single crystals. **c,** Time slices at 15 ns from data (dotted lines) and model (solid lines) showing no significant difference in the spread of carriers for all single crystals. **d,** Diffusivity (red bars) and diffusion lengths (blue bars) for all crystals. Error bars represent 95% confidence intervals of the diffusivity value fits.

diffusion length for MAPbI$_3$ single crystals were determined to be $0.55 \pm 0.02$ cm$^2$ s$^{-1}$ and $0.76 \pm 0.04$ μm, respectively, at an excitation density of $2.4 \times 10^{18}$ carriers per cm$^3$, a result that agrees well with literature-reported values[28,29,32–35].

**Carrier diffusion in perovskites as a function of composition**
TPLM was used to study carrier dynamics in perovskite single crystals of different compositions. We grew single crystals of MA, CsMAFA and CsFA—the compositions most widely used in PSCs (see Methods for details). X-ray diffraction (XRD) of the ground crystals showed pure phase without observable secondary contamination for each of these crystals (Supplementary Fig. 9). MA, CsMAFA and CsFA single crystals showed PL peaks at 1.60, 1.62 and 1.64 eV, respectively (Supplementary Fig. 9). The normalized TPLM data and model results for the CsMAFA and CsFA single crystals are shown in Fig. 2a and Fig. 2b, respectively. Strikingly, there was no significant difference in the temporal evolution of spatial profiles for the three crystal compositions studied (Fig. 2c). As shown in Fig. 2d, the extracted diffusivity values and calculated diffusion lengths for the single crystals also show no appreciable difference despite the widely observed superior PV performance of mixed perovskite compositions (such as CsMAFA)[20,22]. This puzzling result prompted us to look at carrier diffusion in thin films—the sample architecture in which CsMAFA has shown better performance than the other compositions.

We prepared perovskite films of various compositions by solvent engineering[36], a method widely used in the fabrication of high-performance PSCs. XRD of these films revealed a pure perovskite phase (Supplementary Fig. 10). Surface scanning electron microscopy (SEM) and atomic force microscopy images indicate identical grain sizes and roughness in CsMAFA and CsFA films, while MAPbI$_3$ films exhibited a smaller grain size (Supplementary Fig. 10). PSCs based on mixed perovskite films exhibited 20% PCE (Supplementary Fig. 11).

We note that MA and CsMAFA single crystals were synthesized from solute stoichiometries chosen to correspond to the stoichiometries within the final thin films. The CsFA solution for crystal growth had ~5% more iodine than the corresponding CsFA solution for thin films; this is due to the solubility limit of precursors in gamma-butyrolactone (GBL) solvent used for crystal growth. Using GBL also led to a slight increase of Cs and Br content in CsFA and CsMAFA crystals, as seen in elemental analysis and PL studies (Supplementary Table 3 and Supplementary Figs. 9 and 10). Nevertheless, the principle of choosing control samples remained as follows: all CsFA samples had no MA, and were used as counter-control samples to MA-containing samples, such as MA and CsMAFA.

Figure 3a and Fig. 3b show a comparison of TPLM data for CsMAFA single crystal and thin film samples, respectively. The carrier distributions of the single crystal and thin film with model fits at 30 ns are shown in Fig. 3c. The FWHM of the single crystal increased (+2.95 μm) by nearly four times that of the film (+0.75 μm) in that time, compared with the respective FWHM at time zero, indicating that diffusion of carriers is heavily modified in the thin film environment, in agreement with previous findings[37].
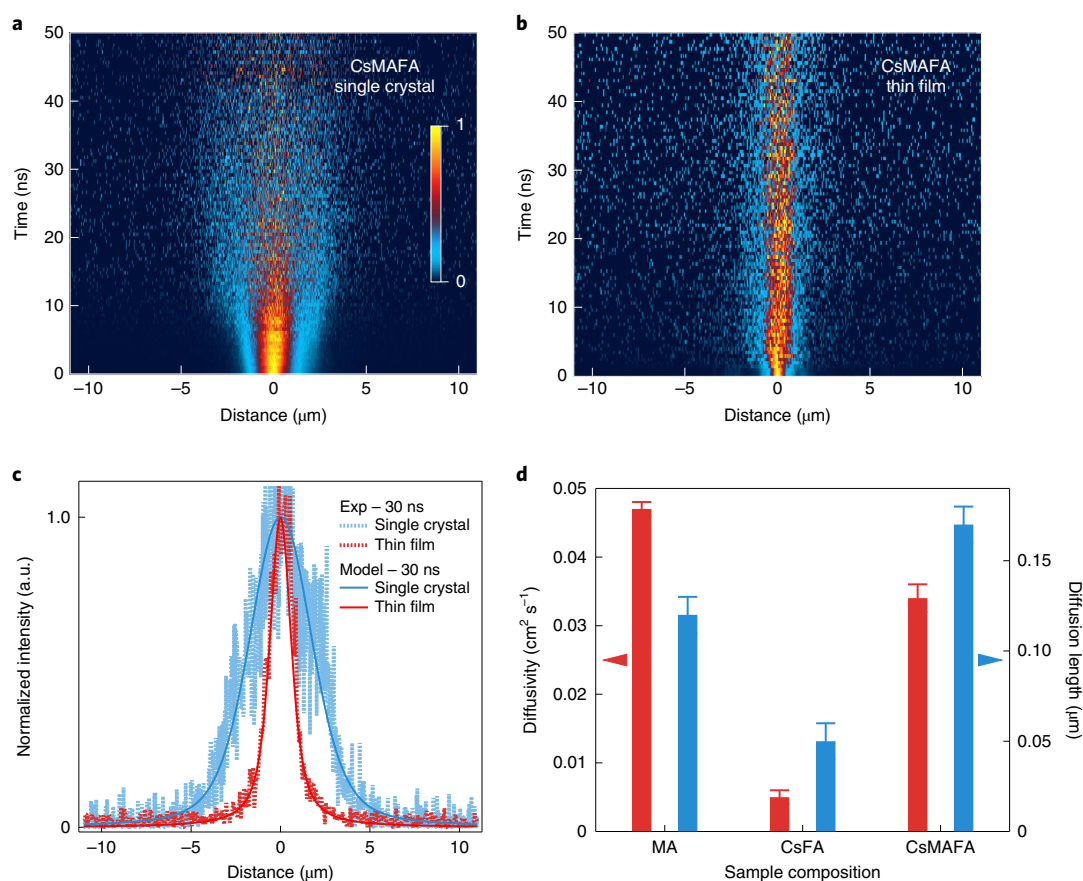
**Fig. 3 | Carrier diffusion of perovskite thin films. a,b** Experimental diffusion images of CsMAFA single crystal (**a**) and thin films (**b**). **c**, Comparison of single crystal and thin film carrier distributions at $30 \pm 5$ ns from the experiment (dotted lines) and model (solid lines). **d**, Diffusivity (red bars) and diffusion lengths (blue bars) for all perovskite thin films. Error bars represent 95% confidence intervals of the diffusivity value fits.

A comparison of diffusivities and diffusion lengths for each film composition is shown in Fig. 3d. Here, we observed a significant composition dependence of these values. The MA film showed the highest diffusivity, while CsFA had a 10× lower diffusivity. Incorporation of MA (such as CsMAFA film) improves the diffusivity by an order of magnitude, yet it is still lower than that of the MA film. Nevertheless, CsMAFA exhibits the longest carrier diffusion length, principally due to its longer carrier lifetime, clarifying the need to include MA to achieve high-performance perovskite compositions[22]. This result also highlights the importance of considering not only how quickly carriers move in a material, but also how long they remain available for collection, when designing better solar materials. The trends in the diffusivities of the thin films were further confirmed by PL quenching experiments (Supplementary Method 2.1 and Supplementary Table 2). The magnitude of the diffusivities agrees well with literature values (Supplementary Table 4).

The emergence of variability in the diffusion of carriers in films may originate from a difference in the in-grain transport or between-grain transfer of the various perovskite compositions. The laser spot size is larger than the grain size, and does not resolve in-grain diffusion in the films[38]; we instead use single crystal studies to reveal in-grain transport and rule out a dominant role for differences in in-grain transport in light of the invariance observed in single crystals. Comparison of transport in perovskite single crystals versus thin films of the same composition (Fig. 3c) showed that the FWHM of the single crystal increased more than that of the film in the same time after excitation, indicating that transport among grains is the limiting factor for carrier movement in the thin films.

## Carrier dynamics in mixed perovskites

The limited carrier transport across grain boundaries in mixed perovskite films can occur because of a high trap density, or due to an energetic barrier[38–40] at the grain boundaries (Fig. 4a). Higher PL intensities from mixed perovskites compared with MA-only films exclude the presence of a high trap density on the surface of grains.

To address the potential energetic barrier on the surface of grains, we performed KPFM, transient photocurrent and PL quenching studies. The average contact potential difference (CPD) values for CsMAFA and CsFA are 16.5 and −57 mV, respectively. To compare the two samples at different positions, we subtract the CPD at each point from the average CPD (Fig. 4d,e). The resultant KPFM images show increased potential variation among grains in CsFA compared with CsMAFA, despite having the same surface roughness (Fig. 4a–c). Depth-profile ultraviolet photoelectron spectroscopy (UPS) shows that the valence band maximum upshifts on the surface of CsFA film. The increasing Br content on the surface of the grain increases the bandgap; therefore, the conduction band minimum upshifts as well, creating an energy barrier for electrons (Supplementary Fig. 13)[41,42]. The picture of the potential energy barrier is further supported by photocurrent decay: it is fastest in MA solar cells, slows in CsMAFA and is slowest in CsFA (Fig. 4f).

To further explore the origins of the energetic barrier on the surface of films and between grains, we acquired elemental composition information on the films. Angle-dependent XPS shows a higher content of Br on the surface of CsFA grains than in CsMAFA films (Fig. 5b). The surface carrier dynamics obtained using transient reflection spectra[31] indicate the same dynamics for the front
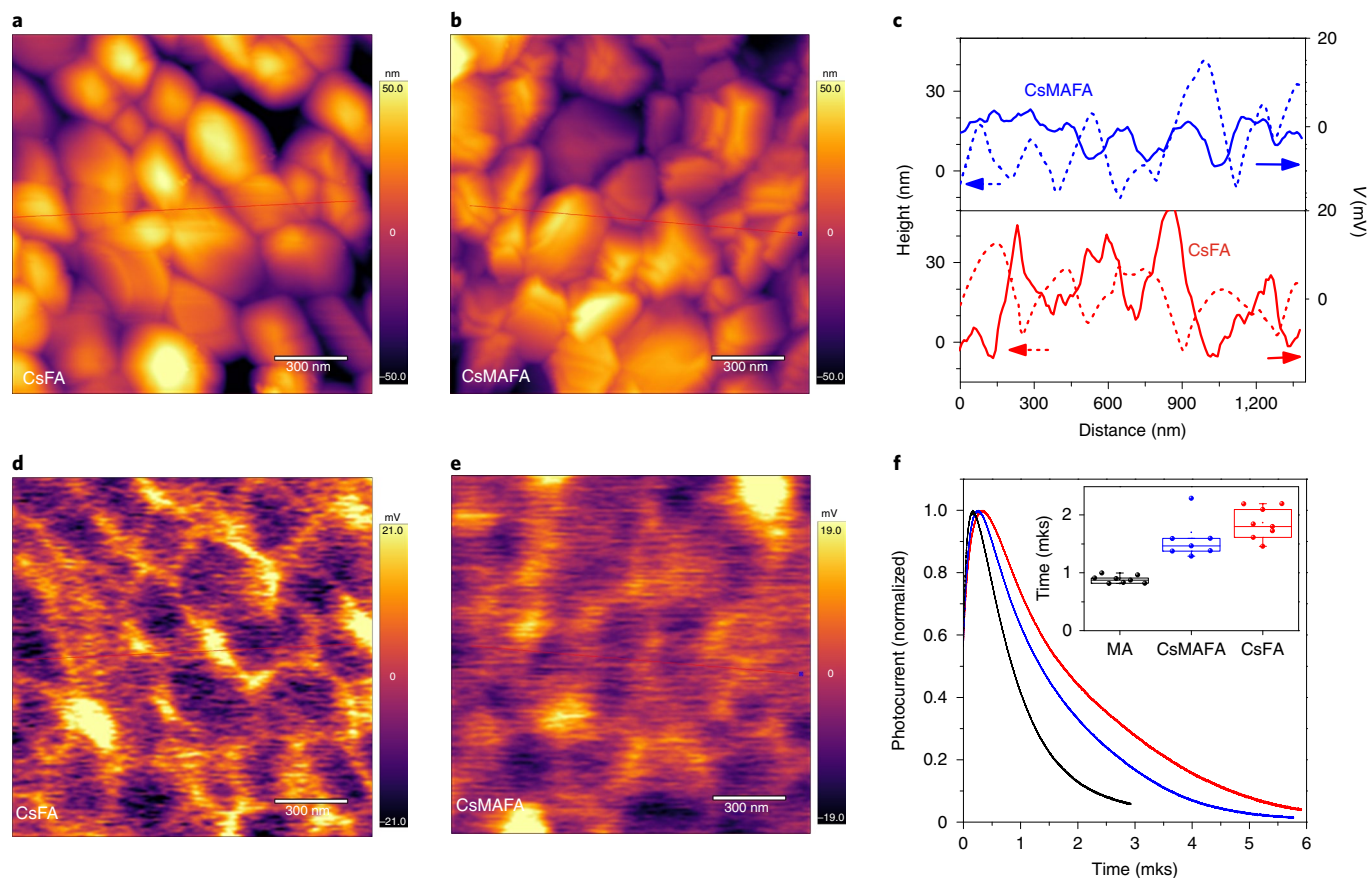
**Fig. 4 | Surface potential and vertical charge transfer studies in perovskite films. a,b,d,e,** KPFM topography map (**a,b**) and CPD map (**d,e**) of mixed perovskite films on ITO. **c,** topography and CPD linescan spectra for corresponding films, demonstrating high CPD variations in CsFA films. **f,** Transient photocurrent traces of corresponding solar cells demonstrating long photocurrent decay in mixed perovskite-based cells. The inset represents statistics from seven independent measurements of transient photocurrent traces. mks, microsecond.

and back of the CsMAFA film and for the front of the CsFA film (Supplementary Fig. 14); however, the CsFA back surface shows longer dynamics, probably due to a different surface composition. The aforementioned angle-dependent XPS and depth-profile UPS analyses support the change of composition from the surface of CsFA film into its bulk. An EDX linescan across grain (reference) and grain boundaries (region of interest) confirms the presence of a Br-rich region at the grain boundaries as compared with grain core (Fig. 5c). The high Br content of this grain 'shell' produces a perovskite with a higher bandgap than the grain core, supporting the picture of an energetic barrier in CsFA films.

**Inhomogeneous crystallization of mixed perovskites**
We account for the observed inhomogeneous grains through the competing crystallization processes in a mixed perovskite solution. A given mixed perovskite solution (left side of equation (3)) would be in equilibrium with a given mixed perovskite phase (first term on the right side of the equation) plus any additional excess pure halide perovskite (remaining terms on the right side of the equation):

$$APb(Br_yI_{1-y})_3 = aAPb(Br_xI_{1-x})_3 + bAPbBr_3 + cAPbI_3 \qquad (3)$$
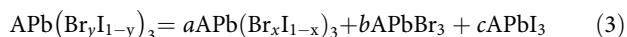
where, if $x > y$, Br is the limiting halide thus inhibiting all Br perovskite, so $b = 0$. Likewise, if $x < y$, I is the limiting halide thus inhibiting all I perovskite, so $c = 0$. The abovementioned equilibrium can be used to calculate the maximum yield, $a$, of a given mixed perovskite $aAPb(Br_xI_{1-x})_3$ for a mixed solution $APb(Br_yI_{1-y})_3$.

The stoichiometry of this reaction implies that its theoretical yield (the maximum possible $a$ coefficient) is controlled by the content of the limiting halogen (see Supplementary Fig. 15 for more details). Figure 5d shows the results of analytical solutions of estimated theoretical yield ($a$) for all possible $APb(Br_xI_{1-x})_3$ (where $x$ varies from 0 to 1) in several given compositions ($y$). While a single halide perovskite solution only forms a single composition (demonstrated as a dot for $y = 0$ in Fig. 5d), mixed perovskites allow for a distribution of varied compositions. This distribution gets wider with a higher degree of mixing ($y \rightarrow 0.5$); the wider the distribution, the higher the probability of forming a gradient during crystallization.

The distribution of halogens in solution does not directly determine the distribution in a crystal. Crystallization in a solution occurs when the distribution shown in Fig. 5d exceeds the solubility. Under the assumption that solubility of all perovskite phases is equal, the distribution of halogens in a mixed perovskite crystal can be determined by a statistical model of combinations with repetition (Supplementary Fig. 16). This model finds that this distribution will depend on the size of the crystal. The distribution linewidth becomes narrower as the size of the crystal is increased, such that a single crystal should exhibit a perfectly narrow distribution centred at the solution ratio $APb(Br_yI_{1-y})_3$, thus explaining our results on single crystals.

The situation varies if the assumption of equal solubility of perovskite phases is not met. We measured the solubility of mixed perovskites (Supplementary Fig. 17 shows the powder XRD of perovskites used for solubility tests) in 4:1 mixture of
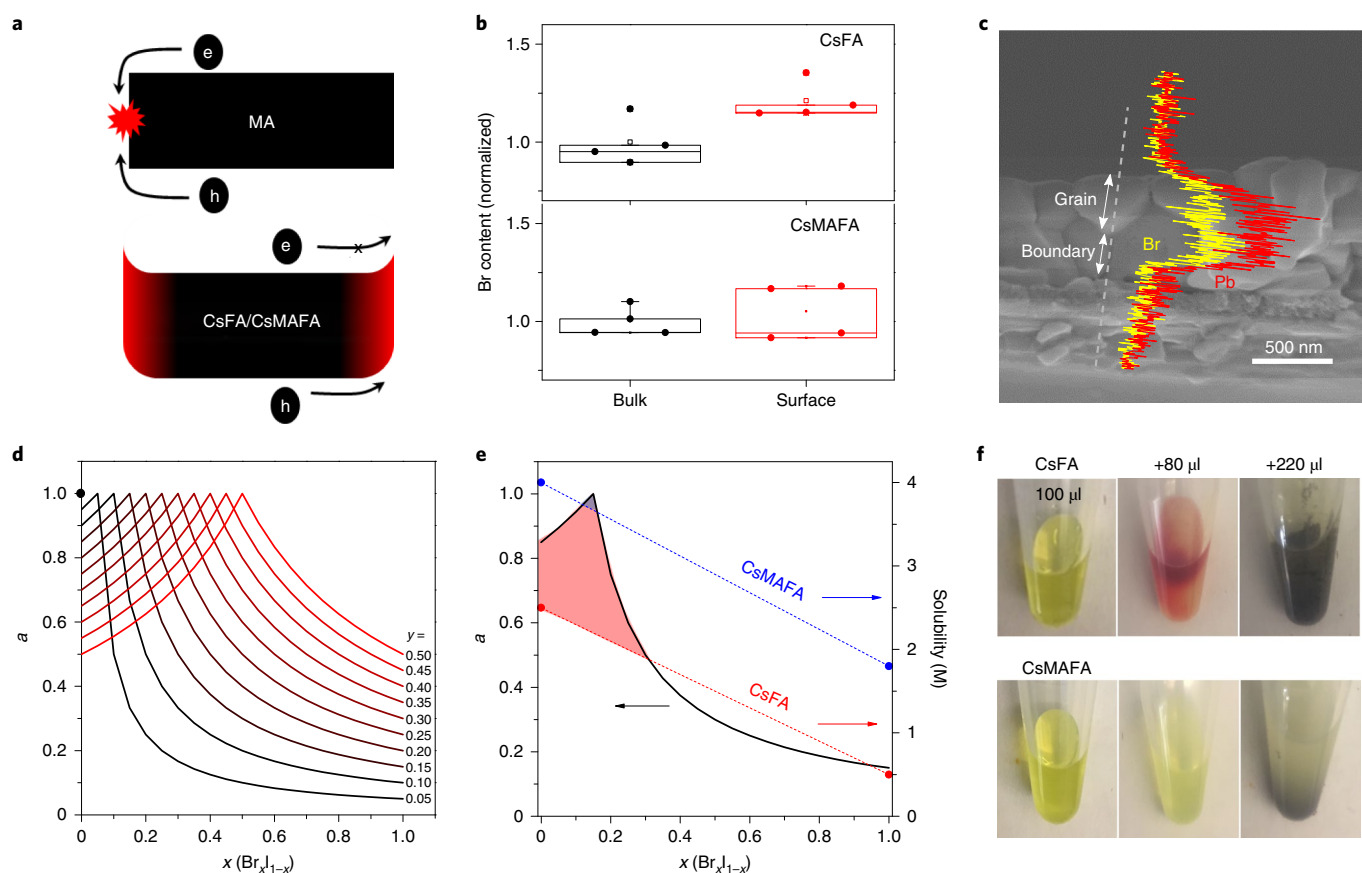
**Fig. 5 | Grain formation in perovskites. a**, Schematics demonstrating the effect of trap densities (top panel) and gradient composition (bottom panel) on carrier diffusivity; in the bottom panel the core of grain is made of small-bandgap perovskite, and the shell is made of wide-bandgap perovskite. **b**, Angle-dependent XPS showing high Br content (normalized to Br content in the bulk) on the surface (60–70° from the normal to the surface) compared with the bulk (25–35° from the normal). The boxes indicate the 25th and 75th percentiles. The median and mean are represented by the line dividing the boxes and the open square symbols, respectively. **c**, EDX linescan mapping showing high Br content. **d**, Compositional distribution in given perovskite solutions. **e**, The effect of solubility on the distribution of crystallized perovskites. **f**, Kinetics of formation of perovskites; CsFA first forms red wide-bandgap perovskite, while CsMAFA forms directly black perovskite. e, electron; h, hole.

N,N-dimethylformamide (DMF)/dimethylsulfoxide, a commonly used solvent system for fabrication of perovskite films of device grade. I-only CsMAFA exhibited a solubility of 4 M, while the corresponding Br-only CsMAFA exhibited a solubility of 1.8 M, less than half of the I-only composition above (Fig. 5e). Such a difference in solubility results in inhomogeneous crystallization of compositions, the shaded region in Fig. 5e for CsMAFA.

We also measured the solubility of the corresponding CsFA perovskites. I-only CsFA exhibited a solubility of 2.5 M, while its corresponding Br perovskite exhibited 5× less solubility (0.5 M). Such a decrease in solubility when moving from I to Br, along with the significantly low solubility of CsFA compared with CsMAFA, results in a wider compositional gradient (shaded region in Fig. 5e)—and therefore limited carrier diffusion—in CsFA thin films.

The picture of inhomogeneous crystallization suggests that if supersaturation is reached quickly, one can isolate Br-rich perovskites. We added antisolvent (chloroform) into perovskite solutions to induce rapid crystallization. The CsMAFA solution directly formed black perovskite (Fig. 5f). However, the CsFA solution formed black perovskite only following the formation of a red precipitate. The red precipitate was isolated and identified by XRD and XPS to be Cs- and Br-rich perovskite (Supplementary Fig. 18). Such a wide distribution in the Cs and Br content of CsFA perovskite explains the presence of an energy barrier between grains and, thus, the lower PCE of corresponding devices compared with MA and CsMAFA PSCs[43].

## Outlook

Transient PL microscopy revealed the emergence of composition-dependent transport in perovskite thin films. Using EDX and XPS, we found that the grains form with a gradient composition in CsFA perovskite thin films, exhibiting Br-rich perovskite regions on the surface of grains. This creates a barrier to electron egress, as seen by KPFM, PL quenching and transient photocurrent ($J_{sc}$) studies. Crystallization dynamics demonstrate that mixed perovskites and the difference in solubility of Br- and I-containing compounds cause this inhomogeneous crystallization. This study implies that flattening the solubility of the most and least soluble components is key in developing next-generation compositions. Avoiding Br in MA-free RbCsFA perovskite shows homogeneous crystallization (Supplementary Fig. 18), thus explaining the high PCE obtained for RbCsFA PSCs[44], but also decreases the bandgap. Next-generation, tandem-cell-compatible perovskites will contain some Br to have a wide bandgap; it will, therefore, be important to develop solvent systems and additives that enhance the solubility of Br-containing components of perovskites.

## Online content

Any methods, additional references, Nature Research reporting summaries, source data, extended data, supplementary information, acknowledgements, peer review information; details of author contributions and competing interests; and statements of data and

## References

1. Kojima, A., Teshima, K., Shirai, Y. & Miyasaka, T. Organometal halide perovskites as visible-light sensitizers for photovoltaic cells. *J. Am. Chem. Soc.* **131**, 6050–6051 (2009).
2. Im, J.-H., Lee, C.-R., Lee, J.-W., Park, S.-W. & Park, N.-G. 6.5% efficient perovskite quantum-dot-sensitized solar cell. *Nanoscale* **3**, 4088 (2011).
3. Kim, H.-S. et al. Lead iodide perovskite sensitized all-solid-state submicron thin film mesoscopic solar cell with efficiency exceeding 9%. *Sci. Rep.* **2**, 591 (2012).
4. Lee, M. M., Teuscher, J. J., Miyasaka, T., Murakami, T. N. & Snaith, H. J. Efficient hybrid solar cells based on meso-superstructured organometal halide perovskites. *Science* **338**, 643–647 (2012).
5. Burschka, J. et al. Sequential deposition as a route to high-performance perovskite-sensitized solar cells. *Nature* **499**, 316–320 (2013).
6. *Best Research-Cell Efficiency Chart* (NREL, accessed 10 October 2019); https://www.nrel.gov/pv/cell-efficiency.html
7. deQuilettes, D. W. et al. Impact of microstructure on local carrier lifetime in perovskite solar cells. *Science* **348**, 683–686 (2015).
8. Hou, Y. et al. A generic interface to reduce the efficiency-stability-cost gap of perovskite solar cells. *Science* **358**, 1192–1197 (2017).
9. Guo, Z. et al. Long-range hot-carrier transport in hybrid perovskites visualized by ultrafast microscopy. *Science* **356**, 59–62 (2017).
10. Davies, C. L. et al. Bimolecular recombination in methylammonium lead triiodide perovskite is an inverse absorption process. *Nat. Commun.* **9**, 293 (2018).
11. Abdi-Jalebi, M. et al. Maximizing and stabilizing luminescence from halide perovskites with potassium passivation. *Nature* **555**, 497–501 (2018).
12. Tsai, H. et al. High-efficiency two-dimensional Ruddlesden–Popper perovskite solar cells. *Nature* **536**, 312–316 (2016).
13. Dastidar, S. et al. High chloride doping levels stabilize the perovskite phase of cesium lead iodide. *Nano Lett.* **16**, 3563–3570 (2016).
14. Cho, H. et al. Overcoming the electroluminescence efficiency limitations of perovskite light-emitting diodes. *Science* **350**, 1222–1225 (2015).
15. Wang, T. et al. Indirect to direct bandgap transition in methylammonium lead halide perovskite. *Energy Environ. Sci.* **10**, 509–515 (2017).
16. Schulz, P. et al. Electronic level alignment in inverted organometal perovskite solar cells. *Adv. Mater. Interfaces* **2**, 1400532 (2015).
17. Pellet, N. et al. Mixed-organic-cation perovskite photovoltaics for enhanced solar-light harvesting. *Angew. Chem. Int. Ed. Engl.* **53**, 3151–3157 (2014).
18. Li, Z. et al. Stabilizing perovskite structures by tuning tolerance factor: formation of formamidinium and cesium lead iodide solid-state alloys. *Chem. Mater.* **28**, 284–292 (2016).
19. McMeekin, D. P. et al. A mixed-cation lead mixed-halide perovskite absorber for tandem solar cells. *Science* **351**, 151–155 (2016).
20. Saliba, M. et al. Cesium-containing triple cation perovskite solar cells: improved stability, reproducibility and high efficiency. *Energy Environ. Sci.* **9**, 1989–1997 (2016).
21. Jeon, N. J. et al. Compositional engineering of perovskite materials for high-performance solar cells. *Nature* **517**, 476–480 (2015).
22. Tan, H. et al. Dipolar cations confer defect tolerance in wide-bandgap metal halide perovskites. *Nat. Commun.* **9**, 3100 (2018).
23. Yang, W. S. et al. Iodide management in formamidinium-lead-halide–based perovskite layers for efficient solar cells. *Science* **356**, 1376–1379 (2017).
24. Lin, K. et al. Perovskite light-emitting diodes with external quantum efficiency exceeding 20 per cent. *Nature* **562**, 245–248 (2018).
25. Correa-Baena, J.-P. et al. Homogenized halides and alkali cation segregation in alloyed organic-inorganic perovskites. *Science* **363**, 627–631 (2019).
26. Dang, H. X. et al. Multi-cation synergy suppresses phase segregation in mixed-halide perovskites. *Joule* **3**, 1746–1764 (2019).
27. Akselrod, G. M. et al. Visualization of exciton transport in ordered and disordered molecular solids. *Nat. Commun.* **5**, 3646 (2014).
28. Shi, D. et al. Low trap-state density and long carrier diffusion in organolead trihalide perovskite single crystals. *Science* **347**, 519–522 (2015).
29. Dong, Q. et al. Electron-hole diffusion lengths >175 μm in solution-grown CH3NH3PbI3 single crystals. *Science* **347**, 967–970 (2015).
30. Pazos-Outon, L. M. et al. Photon recycling in lead iodide perovskite solar cells. *Science* **351**, 1430–1433 (2016).
31. Yang, Y. et al. Top and bottom surfaces limit carrier lifetime in lead iodide perovskite films. *Nat. Energy* **2**, 16207 (2017).
32. Ščajev, P. et al. Two regimes of carrier diffusion in vapor-deposited lead-halide perovskites. *J. Phys. Chem. C Nanomater. Interfaces* **121**, 21600–21609 (2017).
33. Guo, Z., Manser, J. S., Wan, Y., Kamat, P. V. & Huang, L. Spatial and temporal imaging of long-range charge transport in perovskite thin films by ultrafast microscopy. *Nat. Commun.* **6**, 7471 (2015).
34. Xing, G. et al. Long-range balanced electron- and hole-transport lengths in organic-inorganic CH3NH3PbI3. *Science* **342**, 344–347 (2013).
35. Stranks, S. D. et al. Electron-hole diffusion lengths exceeding 1 micrometer in an organometal trihalide perovskite absorber. *Science* **342**, 341–344 (2013).
36. Jeon, N. J. et al. Solvent engineering for high-performance inorganic–organic hybrid perovskite solar cells. *Nat. Mater.* **13**, 897–903 (2014).
37. Delor, M., Weaver, H. L., Yu, Q. & Ginsberg, N. S. Imaging material functionality through 3D nanoscale tracking of energy flow. *Nat. Mater.* **19**, 56–62 (2020).
38. deQuilettes, D. W. et al. Tracking photoexcited carriers in hybrid perovskite semiconductors: trap-dominated spatial heterogeneity and diffusion. *ACS Nano* **11**, 11488–11496 (2017).
39. Yang, M. et al. Do grain boundaries dominate non-radiative recombination in CH₃NH₃PbI₃ perovskite thin films? *Phys. Chem. Chem. Phys.* **19**, 5043–5050 (2017).
40. Arias, D. H., Moore, D. T., Van De Lagemaat, J. & Johnson, J. C. Direct measurements of carrier transport in polycrystalline methylammonium lead iodide perovskite films with transient grating spectroscopy. *J. Phys. Chem. Lett.* **9**, 5710–5717 (2018).
41. Cho, K. T. et al. Highly efficient perovskite solar cells with a compositionally engineered perovskite/hole transporting material interface. *Energy Environ. Sci.* **10**, 621–627 (2017).
42. Luo, D. et al. Enhanced photovoltage for inverted planar heterojunction perovskite solar cells. *Science* **360**, 1442–1446 (2018).
43. Shin, S. S. et al. Colloidally prepared La-doped BaSnO₃ electrodes for efficient, photostable perovskite solar cells. *Science* **6620**, 167–171 (2017).
44. Turren-Cruz, S.-H., Hagfeldt, A. & Saliba, M. Methylammonium-free, high-performance, and stable perovskite solar cells on a planar architecture. *Science* **362**, 449–453 (2018).

## Methods

**Chemicals.** Lead (II) iodide ultra dry 99.999% (metals basis) and lead (II) bromide 99.998% (metals basis) were purchased from Alfa Aesar. Caesium iodide 99.999% (trace metals basis), GBL ≥99%, dimethylsulfoxide anhydrous ≥99.9%, DMF anhydrous 99.8%, chlorobenzene anhydrous 99.8% and chloroform anhydrous ≥99% were purchased from Sigma Aldrich. Formamidinium iodide (FAI) and methylammonium bromide (MABr) were purchased from Greatcell Solar. All chemicals were used as received.

**Preparation of single crystals.** $MAPbI_3$, $Cs_{0.05}MA_{0.15}FA_{0.8}PbI_{2.55}Br_{0.45}$ (CsMAFA) and $Cs_{0.1}FA_{0.9}PbI_{2.7}Br_{0.3}$ (CsFA) crystals were synthesized from 1 M $MAI/PbI_2$ (1:1 molar ratio) solution in GBL, 1 M $CsI/MABr/FAI:PbI_2/PbBr_2$ (0.05:0.15:0.8:0.85:0.15 molar ratio) solution in GBL and 0.9 M $CsI/FAI/PbI_2/PbBr_2$ (0.1:0.9:0.85:0.15 molar ratio) solution in GBL, respectively, using inverse temperature crystallization reported elsewhere[45–47]. Typical dimensions of these crystals were ~3 mm wide × ~2 mm thick.

**Preparation of perovskite thin films.** The corresponding thin films were spin-coated from 1.4 M solution in a mixed solvent of DMF and dimethylsulfoxide (volume ratio 4:1). The perovskite films were deposited in a glovebox with two-step spin-coating procedures: the first step was 1,000 r.p.m. for 10 s with an acceleration of 200 r.p.m. s$^{-1}$; the second step was 5,000 r.p.m. for 60 s with a ramp-up of 1,000 r.p.m. s$^{-1}$. Then, 200 μl of chlorobenzene was dropped on the spinning substrate at 30 s before the end of the second step. The substrate was then annealed at 100 °C for 30 min.

**Solubility.** To test solubility, we first prepared perovskite powders. Mixtures were dissolved in a dimethylsulfoxide/DMF solvent mixture until formation of a transparent solution. Then, a 10× larger volume of chloroform was used to precipitate perovskites. The resultant powders were dried under vacuum for 24 h. The yields were 86%, 77%, 57% and 63% for CsFA-I, CsMAFA-I, CsFA-Br and CsMAFA-Br, respectively.

**Fabrication of PSCs.** Patterned indium tin oxide- (TFD Devices) coated glass was cleaned using acetone and then isopropanol. The $SnO_2$ electron transport layers were spin-coated on indium tin oxide substrates from the colloidal $SnO_2$ nanocrystal solutions at a spin speed of 3,000 r.p.m. for 20 s, and then annealed on a hotplate at 150 °C for 30 min in air. The perovskite films were deposited following the aforementioned procedure. We then spin-coated the hole-transport layer at 4,000 r.p.m. for 20 s (2,000 r.p.m. ramp) from a chlorobenzene solution containing 65 mg ml$^{-1}$ Spiro-OMeTAD, 20 μl ml$^{-1}$ t-butylpyridine and 70 μl ml$^{-1}$ bis(trifluoromethane)sulfonimide lithium salt (170 mg ml$^{-1}$ in acetonitrile). A 120 nm gold was evaporated with an Angstrom Engineering electron-beam deposition system.

**Characterization of solar cells.** The current–voltage (J–V) characteristics of solar cells were measured with a Keithley 2400 sourcemeter in a nitrogen atmosphere (50 mV s$^{-1}$ scanning rate, 10 mV step and 200 ms delay time). The light (100 mW cm$^{-2}$) was generated by a solar simulator (Newport, Class A). To measure stabilized power output, the current density was traced at maximum power point voltage ($V_{MPP}$), determined from the J–V curve. An aperture shade mask (0.049 cm$^2$) placed in front of the solar cell determined the active area. External quantum efficiency (EQE) measurements were performed using a Newport-calibrated ORIEL QuantX 300. Transient photocurrent decays were measured on a home-made system. A continuous light source from an Xe lamp was coupled through a fibre to collimate on the active area of the solar cell.

**Other characterization.** SEM micrographs were obtained using the Hitachi S-5200 microscope (1 kV for SEM images and 5 kV for EDX). XRD analysis was performed using a Rigaku MiniFlex 600 diffractometer (NaI scintillation counter and Cu Kα radiation with wavelength $λ = 1.5406$ Å). XPS analysis was carried out using Thermo Fisher Scientific Thetaprobe XPS. Optical absorption and PL measurements were carried out in a Lambda 950 UV/Visible spectrophotometer and a Horiba Fluorolog time-correlated single-photon-counting system, respectively. The transient reflection spectroscopy characterization method has been performed according to previous works (ref. [48]) and reproduced here for completeness. Femtosecond laser pulses of 1,030 nm generated by a Yb:KGW laser at a 5 kHz repetition rate (Pharos (Light Conversion)) were passed through an optical parametric amplifier (Orpheus (Light Conversion)) selected for 480 nm light. The latter served as the pump pulse, whereas the probe pulse was generated by focusing the initial 1,030 nm pulse into a sapphire crystal, which resulted in a white-light continuum (Helios (Ultrafast)). With a temporal resolution of the system of ~350 fs, each time step meant delaying the probe pulse with respect to the pump, with time steps that increased exponentially. Every other pump pulse was blocked with a chopper to determine the change in optical density. After going through a grating spectrograph, the pulses were measured by means of a charge-coupled device (Helios (Ultrafast)). Multiple scans were taken for each sample at each power, and the average of these scans was used.

**KPFM.** KPFM measurements were performed using an Asylum Research Cypher system in an amplitude modulation lift mode in air to obtain topographical and CPD images. The CPD value was subtracted by the average CPD value of the image. The lift height was 20 nm. All measurements were performed using conductive Ti/Ir-coated atomic force microscopy probes (ASYELEC, Electrolever from Asylum Research) with nominal mechanical resonance frequency and a spring constant of 70 kHz and 2.0 N m$^{-1}$, respectively. The perovskite films studied were fabricated in an ITO/$SnO_2$/perovskite architecture (where ITO is indium tin oxide), and the samples were ground during the measurement.

Ultraviolet photoelectron spectroscopy (UPS) was carried out using an ESCALAB 250Xi system (Thermo Fisher Scientific). Photoelectrons were excited by an ultraviolet discharge lamp with a photon energy of He I line (21.22 eV). Subsequent to each UPS, a short session of ion etching was run in which a beam of low-energy unreactive argon ions (2 keV) scanned 5 × 5 mm$^2$ of the surface for gentle removal of the layers. An argon cluster was used to prevent in-depth damage of the material. When we repeated the mentioned cycle several times, we observed a change in valence band maximum and work function of each sample as a function of depth.

**TPLM.** Carrier diffusion imaging was performed using a home-built microscope set-up. Carrier densities were generated using a pulsed laser source (PicoQuant, 405 nm, 125 kHz, 1.5 μJ per pulse, 590 ps FWHM pulse duration) which was sent to the microscope and focused onto the surface of the crystals and films using an objective lens (Nikon, 40×, 0.6 numerical aperture). During experiments, all samples were mounted inside an evacuated microscope cryostat to protect from degradation due to air and water. Epifluorescence from the excited carrier densities was collected by the same objective and further magnified by a ×4 telescopic relay lens (Nikon) attached to the output of the microscope. The image plane of this lens system thus contained a projected image of the excitation spot at a full ×160 magnification.

A fluorescence map of the sample surface was then recorded by raster scanning the image plane with an avalanche photodiode (PicoQuant, τ-SPAD, 150 μm sensor diameter) in one dimension for all TPLM data, excluding Supplmentary Video 1 and selected frames in Fig. 1b which were scanned in two dimensions. The photodiode was mounted on stepper-motor stages (Thorlabs) and attached to the timing electronics (PicoQuant PicoHarp 300) so that time-correlated single-photon counting measurements could be carried out at each x and/or y position of the image. The time-correlated single-photon counting measurements thus provided a time-resolved fluorescence decay at each position point on the fluorescence map.

**Modelling the TPLM experiments.** All experimental data were modelled according to equation (1). Equation (1) was solved using the EFDM. Initial conditions, $N(x, y, z, 0)$, were determined from the data at $t = 0$ ns (see Supplementary Method 1.4). The PL profile at $t = 0$ was fit by a convolution of a Lorentzian line shape with the avalanche photodiode sensor spatial response profile (a step function with 150 μm width). The initial carrier density ($N_0$) was calculated using the reported laser pulse fluence and absorption coefficient, $α = 2.66 × 10^5$ cm$^{-1}$. The EFDM solution of equation (1) yields the carrier density $N(x, y, z, t)$ as a function of space and time. PL intensity was calculated from the model by squaring $N(x, y, z, t)$ with each point in z modified by the probably of escape due to reabsorption (see Supplementary Methods 1.3 and 1.4). The final simulated TPLM signal was recovered by summing over z and convolving with the avalanche photodiode spatial response profile. An all-at-once, multivariate fit of the experimental diffusion images was carried out using this simulated model output to determine parameters D, A, B and C.

**Reporting Summary.** Further information on research design is available in the Nature Research Reporting Summary linked to this article.

## Data availability

The authors declare that the main data supporting the findings of this study are available within the article and its Supplementary information. Extra data are available from the authors upon request.

## References

45. Saidaminov, M. I. et al. Suppression of atomic vacancies via incorporation of isovalent small ions to increase the stability of halide perovskite solar cells in ambient air. *Nat. Energy* **3**, 648–654 (2018).
46. Nazarenko, O., Yakunin, S., Morad, V., Cherniukh, I. & Kovalenko, M. V. Single crystals of caesium formamidinium lead halide perovskites: solution growth and gamma dosimetry. *NPG Asia Mater.* **9**, e373 (2017).
47. Kadro, J. M., Nonomura, K., Gachet, D., Grätzel, M. & Hagfeldt, A. Facile route to freestanding $CH_3NH_3PbI_3$ crystals using inverse solubility. *Sci. Rep.* **5**, 11654 (2015).
48. Quintero-Bermudez, R. et al. Compositional and orientational control in metal halide perovskites of reduced dimensionality. *Nat. Mater.* **17**, 900–907 (2018).

## Author contributions

M.I.S. and K.W. conceived the idea. M.I.S. and M.W. prepared samples and characterized them. K.W. analysed carrier diffusion imaging results and developed the model. A.J., R.Q.B., M.V., A.P., Y.H., J. P., G.W. and S.O.K. assisted with the experiments and discussions. W.A.T. and E.H.S. directed the overall research. M.I.S., K.W., W.A.T. and E.H.S. wrote the manuscript. All authors read and commented on the manuscript.

## Competing interests

The authors declare no competing interests.

## Additional information

**Supplementary information** is available for this paper at https://doi.org/10.1038/s41563-019-0602-2.

**Correspondence and requests for materials** should be addressed to W.A.T. or E.H.S.

**Reprints and permissions information** is available at www.nature.com/reprints.

Corresponding author(s):   Edward H. Sargent

# Solar Cells Reporting Summary

Nature Research wishes to improve the reproducibility of the work that we publish. This form is intended for publication with all accepted papers reporting the characterization of photovoltaic devices and provides structure for consistency and transparency in reporting. Some list items might not apply to an individual manuscript, but all fields must be completed for clarity.

For further information on Nature Research policies, including our data availability policy, see Authors & Referees.

## ▶ Experimental design

**Please check: are the following details reported in the manuscript?**

1. Dimensions

   Area of the tested solar cells
   ☒ Yes ☐ No
   Described in Methods (Characterization of solar cells). The area of device was ~0.049cm^2.

   Method used to determine the device area
   ☒ Yes ☐ No
   Described in Methods (Characterization of solar cells). Optical aperture is used to define the active area.

2. Current-voltage characterization

   Current density-voltage (J-V) plots in both forward and backward direction
   ☒ Yes ☐ No
   Supplementary Figure 11

   Voltage scan conditions
   *For instance: scan direction, speed, dwell times*
   ☒ Yes ☐ No
   Described in Methods (Characterization of solar cells).

   Test environment
   *For instance: characterization temperature, in air or in glove box*
   ☒ Yes ☐ No
   Nitrogen environments; Temperature 25 oC (see Methods, Characterization of solar cells).

   Protocol for preconditioning of the device before its characterization
   ☒ Yes ☐ No
   No preconditioning was used.

   Stability of the J-V characteristic
   *Verified with time evolution of the maximum power point or with the photocurrent at maximum power point; see ref. 7 for details.*
   ☒ Yes ☐ No
   Maximum power point measurements were conducted (Supplementary Fig. 11c)

3. Hysteresis or any other unusual behaviour

   Description of the unusual behaviour observed during the characterization
   ☒ Yes ☐ No
   Solar cells in this work showed negligible hysteresis

   Related experimental data
   ☒ Yes ☐ No
   Supplementary Figure 11

4. Efficiency

   External quantum efficiency (EQE) or incident photons to current efficiency (IPCE)
   ☒ Yes ☐ No
   Supplementary Fig. 11b

   A comparison between the integrated response under the standard reference spectrum and the response measure under the simulator
   ☒ Yes ☐ No
   The integrated Jsc from EQE spectra is consistent with the Jsc from JV measurements (Supplementary Fig. 11).

   For tandem solar cells, the bias illumination and bias voltage used for each subcell
   ☐ Yes ☒ No
   No tandem cells reported in this work

5. Calibration

   Light source and reference cell or sensor used for the characterization
   ☒ Yes ☐ No
   Newport, Class A simulator is used for the measurements (see Methods, Characterization of solar cells).

   Confirmation that the reference cell was calibrated and certified
   ☒ Yes ☐ No
   The light intensity was calibrated by reference solar cell by Newport.

Calculation of spectral mismatch between the
reference cell and the devices under test

☒ Yes
☐ No

Mismatch factor of 1 was used in our measurements.

6. Mask/aperture

Size of the mask/aperture used during testing

☒ Yes
☐ No

0.049 cm2 (see Methods, Characterization of solar cells)

Variation of the measured short-circuit current
density with the mask/aperture area

☐ Yes
☒ No

We haven't measure the cells with apertures of different sizes.

7. Performance certification

Identity of the independent certification laboratory
that confirmed the photovoltaic performance

☐ Yes
☒ No

We did not certify our cells. But CsMAFA control devices were certified and reported
in our previous paper (Science 2017, 355, 722).

A copy of any certificate(s)
*Provide in Supplementary Information*

☐ Yes
☒ No

We did not certify our cells.

8. Statistics

Number of solar cells tested

☒ Yes
☐ No

At least 30 devices for each composition were tested (Supplementary
Figure 11).

Statistical analysis of the device performance

☒ Yes
☐ No

Histograms of efficiency are shown in Supplementary Figure 11.

9. Long-term stability analysis

Type of analysis, bias conditions and environmental
conditions
*For instance: illumination type, temperature, atmosphere
humidity, encapsulation method, preconditioning temperature*

☐ Yes
☒ No

We did not study the stability of our cells. But CsMAFA and CsFA devices were found
stable in our previous papers (Science 2017, 355, 722; Nat. Commun. 2018, 9, 3100).